

## **CFD Studies on the gas-liquid flow in the swirl generating device**

Putra, R. A.; Schäfer, T.; Neumann, M.; Lucas, D.;

Originally published:

March 2018

**Nuclear Engineering and Design 332(2018), 213-225**

DOI: <https://doi.org/10.1016/j.nucengdes.2018.03.034>

Perma-Link to Publication Repository of HZDR:

<https://www.hzdr.de/publications/Publ-26254>

Release of the secondary publication  
on the basis of the German Copyright Law § 38 Section 4.

[CC BY-NC-ND](#)

# CFD Studies on the gas-liquid flow in the swirl generating device

Ryan Anugrah Putra<sup>a,c\*</sup>, Thomas Schäfer<sup>a</sup>, Martin Neumann<sup>b</sup>, Dirk Lucas<sup>a</sup>

<sup>a</sup>Helmholtz-Zentrum Dresden-Rossendorf, Institute of Fluid Dynamics,

Bautzner Landstr. 400, 01328 Dresden, Germany

<sup>b</sup>Technische Universität Dresden, AREVA Endowed Chair of Imaging Techniques in Energy and Process Engineering, 01062 Dresden, Germany

<sup>c</sup> Department of Mechanical & Industrial Engineering, Faculty of Engineering, Gadjah Mada University, Jalan Grafika No. 2, 55281 Yogyakarta, Indonesia

\*Corresponding author.

E-mail address: [r.putra@hzdr.de](mailto:r.putra@hzdr.de)

Phone: 0049 - 351 - 260 2258

E-mail address:

Ryan Anugrah Putra: [r.putra@hzdr.de](mailto:r.putra@hzdr.de)

Thomas Schäfer: [thomas.schaefer@hzdr.de](mailto:thomas.schaefer@hzdr.de)

Martin Neumann: [m.neumann@hzdr.de](mailto:m.neumann@hzdr.de)

Dirk Lucas: [d.lucas@hzdr.de](mailto:d.lucas@hzdr.de)

### *Abstract*

In this work, CFD simulations using the Euler-Euler approach were performed to model the gas-liquid flow in a swirl-generating device. The computational work was based on experiments, which are conducted in a vertical pipe packed with a static swirl element. Measurements of gas volume fractions at several planes within the swirl element were taken using high-resolution gamma-ray computed tomography (HireCT).

The simulations were carried out for the experimental conditions with defined inlet gas volumetric flow rates of 5 and 10 %. The profile of several key parameters (e.g pressure, liquid and gas velocities and gas fraction) are used to understand the flow behavior inside the device. The radial gas phase distribution obtained from the simulations assuming different mono-disperse and bi-modal bubble sizes is compared against the experimental results. The significant influence of the selected bubble sizes on the profile is shown and discussed within this paper. In general, the radial profile of gas fraction is well captured by the CFD simulations except in the transition zone where a significant discrepancy to the experiment is observed.

### *Keywords*

Swirling flow, Multiphase flow, Inline separator, CFD simulation, Euler-Euler model

## 1. Introduction

Gas-liquid swirl-vane separator is used in Boiling Water Reactors (BWRs) to split a two-phase mixture flowing from the reactor core into steam and water (Matsubayashi et al., 2012, Funahashi et al., 2016). It is also used in Thorium Molten Salt Reactor (TMSR) to remove the fission gas (Yin 2016, Chai 2014). A swirl-vane separator is usually equipped with a static swirl generating device which is responsible to generate the centrifugal force for separation process. When the fluid is passing through such device the flow is directed by its geometry to form a swirling flow downstream the device. Since the geometric shape of the devices significantly influences the performance of the separators, a detailed understanding of the hydrodynamic characteristics in the presence of this swirl element is necessary for a successful design and optimization of the separator.

In principle, the corresponding information can be gathered by experimental investigations. However, it might be not possible to obtain the corresponding information from an existing nuclear reactor due to its operational conditions or for safety reasons. Instead, the information on the flow has to rely on laboratory experiments which are often performed in a reduced scale or so-called pilot scale studies. Pilot scale experiments may require significant financial cost and time. Moreover, additional considerations have to be taken into account to ensure the transferability of the results from the pilot scale studies to a full-scale plant. To overcome those limitations a low cost and timesaving method is desirable. Computational Fluid Dynamics (CFD) has the potential to fulfill such aim and can be viewed as a complimentary method to the experiments (Rusche, 2002).

In order to improve the understanding of the gas-liquid flow behavior around the swirl element, one of the important information that needs to be obtained is the cross-sectional gas phase distribution. It is well known that this profile is one of the key parameters to characterize multiphase flow (Azizi et al., 2016; Kanizawa and Ribatski, 2017; Xue et al., 2016; Zhao et al., 2016). However, to the best of the author's knowledge, a systematic CFD study on the gas-liquid flow around the swirl generating device for the prediction of gas fractions is very few in the open literature. The plausible reasons for this scarcity are similar to the one pointed out by (Zidouni et al., 2015) for the case of static mixer: the shortage of suitable experimental data for CFD model validation and the complexity of CFD modeling on multiphase flow. The shortage of the experimental data may root from the difficulty to measure the profile of gas fractions in the complex geometry (Zhu and Zhang, 2016). Such problem may lead to CFD study to estimate gas fractions without comparison to the experimental data. Furthermore, the simulation results may be significantly influenced by the models and set-up selected in the simulation. Moreover, the CFD technology is not yet mature for multi-phase flows modelling (Lucas et al., 2016). Therefore the comparison of the CFD result to the experimental data is highly required.

Focusing the further discussion on the complexity of CFD modeling on gas-liquid flows, the main reason is the complexity of the gas-liquid interface. The scales of these interfaces may reach from very small structures (e.g. microbubbles) to very large ones (e.g. the interface in a stratified flow). On the one hand, the structure of these interfaces determines the interaction between the phases – on the other hand, the structure is determined by these interactions. This complexity probably leads to the CFD study on the gas-liquid flow around the swirl generating

device by simply ignoring the influence of the gas phase (e.g. (Cai et al., 2014). (Yin et al., 2015) conducted numerical studies using Euler-Euler approach assuming a mono-disperse uniform bubble size. However, no information on the quantitative comparison to the experiment on the radial gas distribution profile was presented in the paper. Moreover, the influence of selected bubble size was not investigated in their study. CFD study for estimating the radial profile of gas fractions with a proper comparison to the experimental data has been conducted by (Zidouni et al., 2015). They carried out Euler-Euler CFD simulations on gas-liquid flow in static mixer using a mono-dispersed approach. The influence of selected bubble size was investigated in their study. However, the geometry of swirl generating device either in inline separator or static mixer may widely vary leading to different characteristics of the flow. For example (Yin et al., 2015; Yin et al., 2016) reported that the gas core structure downstream the swirl element is influenced by the flow parameters and geometry of the element. Those factors leads to four types of gas core formation, which were defined by them as: “air core with suction”, “tadpole-shaped core”, “cloudy core” and “rod core”. Therefore, more CFD studies are required to enrich the understanding of the flow characteristics around the swirl generating device.

In this present work, both experimental and CFD studies were performed to investigate the characteristics of the gas-liquid flow around the swirl generating device. A high resolution measuring technique namely high-resolution gamma-ray computed tomography (HireCT) was used to provide the radial gas phase distribution. To explore the physics of the flow, CFD simulations using Euler-Euler approach based on the experiment with defined inlet gas volumetric flow rates of 5 and 10 % were performed. In order to investigate the influence of selected bubble sizes, the simulations were carried out assuming different mono-disperse and bi-modal bubble sizes.

## 2. Experiments

The experiments were carried out at the experimental facility for radiographic imaging at the department of Experimental Thermal Fluid Dynamics, Helmholtz-Zentrum Dresden-Rossendorf (HZDR), Dresden, Germany. The schematic diagram of the experimental facility is shown in **Fig. 1**. Liquid (tap water) is taken using the centrifugal pump Etachrom BC 032-160/074 C11 (KSB, Germany) from a two-stage 600 l separator which ensures the gas separation from the incoming mixture flow. The temperatures of the fluid is kept at 21 °C using a thermostat-controlled heat exchanger C200 301-1 (FUNKE, Germany). The liquid is supplied from the bottom of the test section through a pipe with inner diameter of 25 mm. An in-house developed multi-mode gas injection module was used to inject the gas into the liquid stream via four nozzles arranged symmetrically around the pipe located 12 L/D upstream of the lower edge of the swirl generating device. This injection generates a dispersed gas-liquid flow upstream the device.

An in-house designed static swirl generating device with a length of 82.6 mm and diameter of 27 mm was installed in the vertical test section which has inner diameter of 27 mm. The device consists of four blades that have different structures between their bottom and top parts (see **Fig. 2. (a)** ). The blades in the bottom part are straight vertical plates having the length of 40 mm which are connected in a way that they are oriented orthogonal to each

other. These blades divide the pipe into four equivalent domains. Differently, the blades in the top parts have curvy shape with the blade angle of 20 °.

To adjust the flow rates and the inlet gas phase fractions, an inductive liquid flow meter (MAG 1100, Siemens) and a PID regulated gas flow meter (FMA-2600, OMEGA Newport) are used, respectively. The inlet gas volume fraction  $\varepsilon_{in}$  is defined as

$$\varepsilon_{in} = \frac{Q_G}{Q_G + Q_L}, \quad (1)$$

where  $Q_G$  is the inlet gas flow rate and  $Q_L$  is the liquid flow rate. The experiments were performed for two representative superficial liquid velocities ( $J_L = 2$  and 4.7 m/s) and two representative inlet gas volume fractions ( $\varepsilon_{in} = 5$  and 10 %). In the CFD analysis presented in this work only the test with the inlet gas volume fraction of 5 % and 10 % and the superficial velocity of liquid of 2 m/s was considered.

The measurement of gas distribution at several planes (see **Fig. 2.** (b). and Table 1) within the swirl element region as well as up- and downstream of the element was carried out using HireCT system. The relevant part of the test section used as the domain for CFD simulations in this work together with the axial positions of the measurement planes is presented in **Fig.2.** (b). A detail explanation of the system and the method for data processing can be found in (Hampel et al., 2007; Neumann et al., 2016; Schäfer et al., 2015).

### 3. Computational modeling

Since the nature of the gas-liquid flow around the swirl generating device is three dimensional (3-D) CFD modeling considering 3-D geometry of the test section was performed. Euler-Euler model was selected in this present work since it is the most feasible option for modelling two-phase flow considering practical applications. This model is applicable for all flow regimes and can be used in a very complex flow even when there is no possibility to use another model (Andersson et al., 2012). In this model, two set of governing equations are solved in fixed computational grids and the phase fraction term is introduced into the equation reflecting the existence probability of a certain phase in a certain cell and time (Rusche, 2002).

In the present simulations, both liquid and gas phases are assumed to be adiabatic and incompressible. Governing equations that have to be solved in the calculation across the computational domain are continuity and momentum equations, which have the following forms

$$\frac{\partial}{\partial t}(\alpha_j \rho_j) + \nabla \cdot (\alpha_j \rho_j \mathbf{U}_j) = \mathcal{S}_j \quad (1)$$

$$\frac{\partial}{\partial t}(\alpha_j \rho_j \mathbf{U}_j) + \nabla \cdot (\alpha_j (\rho_j \mathbf{U}_j \times \mathbf{U}_j)) = -\alpha_j \nabla p + \nabla \cdot (\alpha_j \mu_j (\nabla \mathbf{U}_j + (\nabla \mathbf{U}_j)^T)) + M_j + \mathcal{S}_{Mj} \quad (2)$$

In above equations,  $\alpha_j$  denotes the volume fraction,  $\rho_j$  is the density,  $\mathbf{U}_j$  is the velocity vector,  $t$  is the time,  $\mathbf{S}_j$  is the mass source and  $p$  is the pressure. The term of  $\left(\alpha_j \mu_j \left(\nabla \mathbf{U}_j + (\nabla \mathbf{U}_j)^T\right)\right)$  represents the viscous stress tensor. The subscripts  $j$  represents the phase  $j$ .  $\mathbf{M}_j$  is the interfacial forces acting on phase  $j$  due to the presence of other phase while  $\mathbf{S}_{Mj}$  is the momentum sources due to external body forces.

Based on the previous experiences on CFD simulation of adiabatic air-water flow in round pipes (e.g (Lucas et al., 2007; Rzehak and Krepper, 2013a, b)) the set of closure models for bubble forces namely drag, lift, wall and turbulent dispersion forces were used in this work and summarized in the section 3.1. The description of the turbulence model used in this work is presented in the section 3.2. Other aspects including computational setup and boundary conditions are given in the section 3.3.

### 3.1 Bubble forces

#### Drag force

When a bubble moves through the liquid, it experiences a force that resists its motion. This force is called drag force which can be calculated as

$$\mathbf{F}^{drag} = -\frac{3}{4d_B} C_D \rho_L \alpha_G |\mathbf{u}_G - \mathbf{u}_L| (\mathbf{u}_G - \mathbf{u}_L) \quad (3)$$

The according drag coefficient  $C_D$  is calculated based on (Ishii and Zuber, 1979), giving

$$C_{D,bubb} = \max \left( C_{D,sphere}, \min(C_{D,ellipse}, C_{D,cap}) \right) \quad (4)$$

where

$$C_{D,sphere} = \frac{24}{Re} (1 + 0.1 Re^{0.75}) \quad (5)$$

$$C_{D,ellipse} = \frac{2}{3} \sqrt{Eo} \quad (6)$$

$$C_{D,cap} = \frac{8}{3} \quad (7)$$

#### Lift force

The lift force is responsible for the transverse migration of the bubble when it rises in a liquid shear flow. This force that acts perpendicular to the relative motion of the bubble can be expressed by

$$\mathbf{F}^{lift} = -C_L \rho_L \alpha_G (\mathbf{u}_G - \mathbf{u}_L) \times \text{rot}(\mathbf{u}_L) \quad (8)$$

where  $C_L$  is the lift coefficient, which can be determined from the correlations given by (Tomiyama et al., 2002)

$$C_L \begin{cases} \min [0.288 \tanh(0.121 Re), f(Eo_{\perp})] & Eo_{\perp} < 4 \\ f(Eo_{\perp}) & \text{for } 4 < Eo_{\perp} < 10 \\ -0.27 & 10 < Eo_{\perp} \end{cases} \quad (9)$$

$$\text{with } f(Eo_{\perp}) = 0.00105 Eo_{\perp}^3 - 0.0159 Eo_{\perp}^2 - 0.0204 Eo_{\perp} + 0.474 \quad (10)$$

where  $Eo_{\perp}$  is a modified Eötvös number defined as

$$Eo_{\perp} = \frac{g(\rho_L - \rho_G) d_{\perp}^2}{\sigma} \quad (11)$$

Here,  $d_{\perp}$  is the maximum horizontal dimension of the bubble which can be calculated from the correlation given by Wellek et al. (1966):

$$d_{\perp} = d_B \sqrt[3]{1 + 0.163 Eo^{0.757}} \quad (12)$$

### **Wall force**

Wall force acts on a bubble near by a wall and prevents it from touching the wall (Antal et al., 1991). This force can be calculated as:

$$\mathbf{F}^{wall} = \frac{2}{d_B} C_W \rho_L \alpha_G |u_G - u_L|^2 \hat{\mathbf{y}} \quad (13)$$

where  $\hat{\mathbf{y}}$  is the unit normal pointing into the fluid and  $C_W$  is the wall force coefficient. According to (Tomiya et al., 1995) the wall force coefficient  $C_W$  can be calculated as:

$$C_W(y) = f(Eo) \left( \frac{d_b}{2y} \right)^2, \quad (14)$$

Here,  $f(Eo)$  is determined from the correlation given by (Hosokawa et al., 2002):

$$f(Eo) = 0.0217 Eo. \quad (15)$$

### **Turbulent dispersion force**

Turbulent dispersion force is the force experienced by bubbles due to the turbulent fluctuations of the liquid phase. In this work, the Favre Averaged Drag (FAD) model (Burns et al., 2004) for turbulent dispersion was used, where the force is calculated as:

$$\mathbf{F}^{disp} = -\frac{3}{4} C_D \frac{\alpha_G}{d_B} |\mathbf{u}_G - \mathbf{u}_L| \frac{\mu_L^{turb}}{\sigma_{TD}} \left( \frac{1}{\alpha_L} + \frac{1}{\alpha_G} \right) grad \alpha_G \quad (16)$$

The value of the turbulent Schmidt number for the liquid phase is set to  $\sigma_{TD} = 0.9$ .



### 3.2 Turbulence model

The two-equation shear stress transport (SST) model proposed by (Menter, 1994) is used for the liquid phase. In order to take into account the effect of the swirling flow, the curvature correction implemented by (Smirnov and Menter, 2009) was applied in this work. The model uses the empirical function suggested by (Spalart and Shur, 1997), which is given by:

$$f_{rotation} = (1 + c_{r1}) \frac{2r^*}{1+r^*} [1 - c_{r3} \tan^{-1}(c_{r2} \tilde{r})] - c_{r1} , \quad (17)$$

The function is used to control the production term  $P_k$  and is slightly modified in ANSYS CFX (CFX Documentation):

$$P_k \rightarrow P_k \cdot f_r \quad (18)$$

with

$$f_r = \max[0, 1 + C_{scale}(\tilde{f}_r - 1)] \quad (19)$$

and

$$\tilde{f}_r = \max\{\min(f_{rotation}, 1.25), 0\} \quad (20)$$

The arguments  $r^*$  and  $\tilde{r}$  in equation (17) are given by:

$$r^* = \frac{S}{\Omega} \quad (21)$$

and

$$\tilde{r} = 2\Omega_{ik}S_{jk} \left[ \frac{DS_{ij}}{D_t} + (\varepsilon_{imn}S_{jn} + \varepsilon_{jmn}S_{in})\Omega_m^{Rot} \right] \frac{1}{\Omega D^3} \quad (22)$$

The strain rate and vorticity tensor,  $S_{ij}$  and  $\Omega_{ij}$  respectively, are expressed as:

$$S_{ij} = \frac{1}{2} \left( \frac{\partial U_i}{\partial x_j} + \frac{\partial U_j}{\partial x_i} \right) \quad (23)$$

$$\Omega_{ij} = \frac{1}{2} \left( \frac{\partial U_i}{\partial x_j} - \frac{\partial U_j}{\partial x_i} \right) + 2\varepsilon_{mji}\Omega_m^{rot} \quad (24)$$

where

$$S^2 = 2S_{ij}S_{ij} \quad (25)$$

$$\Omega^2 = 2\Omega_{ij}\Omega_{ij} \quad (26)$$

$$D^2 = \max(S^2, 0.09\omega^2) \quad (27)$$

The empirical constants  $c_{r1}$ ,  $c_{r2}$  and  $c_{r3}$  in the equation (17) are set equal to 1.0, 2.0, and 1.0, respectively.

In order to take into account the bubble induced turbulence, additional source terms are added into the turbulence model. The equations for the source terms as well as parameter and coefficient values are defined based on the work of (Rzehak and Krepper, 2013a, b). The source terms for the k-equation and  $\varepsilon$ - equation are given by the following expressions, respectively:

$$S_L^k = F_L^{drag} \cdot (u_G - u_L) \quad (28)$$

$$S_L^\varepsilon = C_{\varepsilon B} \frac{S_L^k}{\tau} \quad (29)$$

where the coefficient  $C_{\varepsilon B}$  is set equal to 1.0 and the time-scale  $\tau$  is defined as:

$$\tau = d_B / \sqrt{k_L} \quad (30)$$

The transformation of  $\varepsilon$ -source to  $\omega$ -source for enabling the use in SST model gives:

$$S_L^\omega = \frac{1}{C_\mu k_L} S_L^\varepsilon - \frac{\omega}{k_L} S_L^k \quad (31)$$

The turbulent viscosity which has already been evaluated due to the inclusion of the bubble induced effects in the k and  $\varepsilon/\omega$  equations is given by:

$$\mu_L^{turb} = C_\mu \rho_L \frac{k_L^2}{\varepsilon_L} \quad (32)$$

### 3.3. Computational setup & boundary conditions

The simulations were performed with ANSYS-CFX 17.2. The gas is treated as an incompressible fluid. The profile for the liquid velocity and turbulent parameters (turbulence kinetic energy and turbulence eddy dissipation) at the inlet are defined according to a previous simulation of fully developed single-phase flow. Mass flow rate boundary giving an equivalent of  $\varepsilon_{in} = 5\%$  and  $\varepsilon_{in} = 10\%$  together with the experimentally determined gas fraction profile before the swirl element is used for gas phase condition at the inlet. A no-slip wall and free-slip wall boundary are used for the liquid and gas phase, respectively. A pressure boundary condition is defined at the outlet of the computational domain. A wall function assuming a smooth wall is used to avoid the need to resolve the viscous sublayer. Simulations are performed without considering any heat transfer (i.e adiabatic).

Unfortunately no information on bubble size was obtained in the experiments. To investigate the influence of selected bubble size used in the simulations, the bubble size ( $d_B$ ) was set to fixed values of 0.5 mm, 1 mm and 2

mm. As an addition, bimodal bubble sizes namely Bimodal\_15% and Bimodal\_30% were also tested to enrich the discussion. Bimodal\_15 % consists of 85 % of  $d_B = 0.5$  mm and 15 %  $d_B = 8$  mm while Bimodal\_30 % consists of 70 % of  $d_B = 0.5$  mm and 30 %  $d_B = 8$  mm. The bubble force models used for  $d_B = 8$  mm are the same as other bubble sizes except for the wall force which was switched-off due to a convergence issue. All simulations were carried out in steady-state mode.

#### 4. Results and discussions

The axial profiles of absolute pressure obtained by averaging over the cross-section of the pipe for  $\varepsilon_{in} = 5$  % and  $\varepsilon_{in} = 10$  % are shown in **Fig. 3. (a)** and **Fig. 4. (a)**. Both profiles show that the pressure drop is higher in the swirl element zone. A relatively drastic reduction of the pressure is observed in the region close to the entrance of the swirl element. Outside the swirl element zone, the slope of pressure curves is in the range of 8-10 Pa mm<sup>-1</sup>. The calculated pressured drops are listed in **Table 2**. Interestingly, there is no significant difference of the calculated pressure drop for  $\varepsilon_{in} = 5$  % and  $\varepsilon_{in} = 10$  %. The results also show that the influence of bubble size on the pressure profile is insignificant.

The axial profiles of the cross-sectional averaged vertical liquid velocity, vertical gas velocity and gas fraction for  $\varepsilon_{in} = 5$  % are presented in **Fig. 3. (b), (c) and (d)**, respectively. The liquid velocity increases when the flow enters the swirl element zone due to the reduction of the cross sectional area caused by the presence of the swirl element. The profile also indicates that the selected bubble size almost has no influence on the axial liquid velocity profile. This condition is also observed in the case of  $\varepsilon_{in} = 10$  % (see **Fig. 4. (b)**). For the axial gas velocity, a strong variation in the profile is observed especially in the region close to the bottom of the swirl element and to the outlet of the computational domain. A significant influence of selected bubble size on the axial gas fraction profile is observed especially in the region close the top part of the element. The average gas fraction in those regions is increased by increasing the selected bubble size. The similar behavior is also observed for the case of  $\varepsilon_{in} = 10$  % ((see **Fig. 4. (c) and (d)**).

**Fig. 5.** and **Fig. 6.** show the streamlines of liquid and gas velocity for  $\varepsilon_{in} = 5$  % and  $\varepsilon_{in} = 10$  %, respectively. Independent from the selected bubble sizes and the inlet gas volume fraction, similar behavior of the streamlines is observed. The smooth straight streamlines of liquid and gas are observed upstream of the swirl element. The swirl flow is not yet formed in region A. From the images of gas fraction (see **Fig. 7.**) it is inferred that the flow in this region is still in the bubbly flow regime. The transition starts downstream when the fluid enters region B. The fluid flow is twisted by following the curvature of the swirl element blades and forms a swirling flow. A wall bounded swirling flow can be observed from the liquid streamlines in region C. In contrast to liquid streamlines, the gas streamlines are concentrated in the center of the pipe due to its lower density. These conditions of flow fields lead to the separation between liquid and gas as can be seen in **Fig. 7.**

The influence of selected bubble sizes on the axial profile of gas fractions especially in region C (i.e. gas core region) can be observed in **Fig. 7.** For both inlet volume fractions, the magnitude of the cross-sectional gas fraction

in this region is increased by the increase of the selected bubble size. This behavior can be attributed to the limitation of mono-dispersed approach. The closure models for bubble force used in the simulations are developed for low gas volume fractions while in this presented simulations locally larger volume fractions are observed within the gas core region (Zidouni et al., 2015). Qualitatively, the gas core thickness obtained from the simulation with  $\varepsilon_{in} = 10\%$  is larger than one with  $\varepsilon_{in} = 5\%$ . To have a quantitative description of gas fraction profile, the remaining part of this section will cover the discussion based on the radial gas distribution over some measurement planes.

The radial gas fraction profiles for the present bubble sizes at the measurement plane H1 for  $\varepsilon_{in} = 5\%$  are presented in **Fig. 8.** The profiles indicate the importance of virtual mass force model for well capturing the distribution of the gas fraction (see **Fig. 8.** (a)). Due to the reduction of the cross-sectional area, bubbles are accelerated while entering region A. Without virtual mass force model, this acceleration cannot be well considered. For all tested bubble sizes, an unrealistic peak of gas fraction is observed near the pipe wall for the simulation without using the virtual mass force. In addition, the profile also shows a strong dependence to the selected bubble size. Among the tested bubble size, the simulation result for  $d_B = 0.5$  mm give the best fit to the experiments. All other bubble sizes under-predict the experiment in the region near to the center of the pipe. A possible explanation is that the collision of bubbles with the bottom part of the swirl element may promote the break-up process resulting in large portion of small bubbles. On the other hand possibly large bubbles are generated by coalescence. To support this argument additional simulation are carried out using bimodal bubble sizes. The result, which is presented in **Fig. 8.** (b), reveals the improvement of gas fraction profile due to bimodal bubble size. It seems that the break-up process does not convert all the bubbles into small bubbles but there is still some portion of large bubbles remain. These large bubbles have a positive lift coefficient that leads them to migrate and occupy the center of each quarter of the element thus maintaining the center peak of the profile.

Since the bimodal bubble size is important to describe the dependence of the radial gas distribution to the bubble size distribution at the inlet then the results of simulations using the bimodal bubble size are plotted altogether with the result of simulations using uniform mono-disperse bubble size for all measurement planes. Those profiles are presented in **Fig. 9.** and **Fig. 10.** for the case of  $\varepsilon_{in} = 5\%$  and  $\varepsilon_{in} = 10\%$ , respectively. The profile of gas fraction at H1 for  $\varepsilon_{in} = 10\%$  is narrower with a peak closer to the center of the pipe than the profile obtained in the case of smaller inlet gas volume fraction. Within this flow condition, the influence of selected bubble size is more pronounced. For example, the application of  $d_B = 1$  mm and  $d_B = 2$  mm in the simulation leads to large deviations of the results from the experimental data. Using bimodal input with 30 % of  $d_B = 8$  mm results in the best agreement of simulation and experiment. However, a significant discrepancy still can be observed from the profile, which indicates that another bubble size distribution may give a better result.

The gas fraction profile derived from the experimental data at plane H2 for  $\varepsilon_{in} = 5\%$  is similar to plane H1. However, there is an increase of gas fraction in the region closer to the inner wall for  $\varepsilon_{in} = 10\%$ . For both cases, the simulations using  $d_B = 0.5$  mm and  $d_B = 1$  mm leads to the accumulation of bubbles near the inner wall in such

1  
2  
3 extent that the gas fractions over-predict the experiment. Similar to the previous measurement plane, the bimodal  
4 input with 30 % of  $d_B = 8$  mm provides the closest accordance to the experimental result for both inlet gas volume  
5 fractions.  
6

7  
8 The profile of gas fraction derived from the experimental data at plane H3, which is in the region B (i.e.  
9 transition region), indicates that the gas phase was already accumulated in the center of the pipe with a maximum  
10 gas fraction of about 20 % and 40 % for the inlet gas volume fraction of  $\varepsilon_{in} = 5$  % and  $\varepsilon_{in} = 10$  %, respectively.  
11 However, this accumulation process seems to be delayed in the simulation. Therefore, the peak of gas fraction in  
12 the simulation is not located precisely in the center of the pipe. A progressive development of the gas core is  
13 observed from the experimental data of the gas fraction at the measurement plane H4. The maximum gas fraction is  
14 increased about 40 % and 35 % compared to the maximum gas fraction at H3 for  $\varepsilon_{in} = 5$  % and  $\varepsilon_{in} = 10$  %, respectively.  
15 However, the simulation results show the similar behavior as in plane H3. The simulation does not yet  
16 able to capture the development of the gas core. Although the maximum peak of gas fraction is already at the center  
17 of the pipe, it is significantly under-predicted. The results also show that the influence of the bubble sizes at this  
18 location has less impact on the gas profile. The inability for capturing the profile in the transition region may be  
19 attributed to the limitation of mono-dispersed approach which is more suitable for the bubbly flow as one found at  
20 the plane H1 and H2. In the transition region, it is possible that both continuous and dispersed gas structures exist.  
21 Here, the closure models of bubble forces applied for bubbly flow are no longer suitable for the continuous gas.  
22

23  
24 The radial gas distribution from the experimental data at the measurement plane H5 shows that the gas core is  
25 somehow weaker than one observed at the plane H4. This phenomenon occurs in both cases, where the maximum  
26 gas fraction at the center of the pipe decreases about 20 %, which may be attributed to the swirl-decaying process  
27 due to the decrease of the centrifugal force. In contrast to the experiment, the gas core in the simulation is  
28 continuously developed. The profile for selected bubble size of 1 and 2 mm largely over-predicts the experiment.  
29 The best-fit result is obtained with the simulation using bimodal 30 % and  $d_B = 0.5$  mm for the case of  $\varepsilon_{in} = 5$  %  
30 and  $\varepsilon_{in} = 10$  %, respectively. The gas core seems not significantly changed at the plane H6 in the experiment while  
31 it is still developed into a stronger one in the simulations. The increase in the peak value of gas fraction is observed  
32 in the simulations for all tested bubble sizes for both inlet gas volume fractions. The bimodal 30 % and  $d_B = 0.5$   
33 mm still provides the closest accordance to the experimental result for the case of  $\varepsilon_{in} = 5$  % and  $\varepsilon_{in} = 10$  %, respectively.  
34 The presence of gas core in region C, which may represent a continuous gas structure probably  
35 requires a better treatment of interface such as an interface capturing model usually used in the simulation of free-  
36 surface flow. Therefore, a new approach that is able to simulate the whole domain of this swirl element, which  
37 consists of the bubbly flow regime in region A, transition regime in region B and also gas core or free-surface  
38 regime in region C is required for a better estimation of gas distribution profiles.  
39  
40  
41  
42  
43  
44  
45  
46  
47  
48  
49  
50  
51  
52  
53  
54  
55  
56  
57  
58  
59  
60  
61  
62  
63  
64  
65

## 5. Conclusions

Gas-liquid flow in a swirl generating device has been investigated for two different inlet gas volume fractions by means of multiphase CFD simulations using the Euler-Euler approach. The flow regimes inside the device can be divided into three regions namely bubbly flow region, transition region and gas core region. In the bubbly flow region, the radial profiles of gas fraction including the peak location obtained from the simulations are highly influenced by the selected bubble size. In the transition region, the profile cannot be well predicted by the simulations and less influenced by the selected bubble sizes. In the gas core region, the magnitude of the maximum gas fraction is increased by the use of a larger bubble size.

Although the gas profile obtained in the simulations is in close agreement to the experiment for a certain selected bubble size, however the decay of gas core cannot be well captured by the simulations. Coalescence and breakup may play role and should be considered in general. However, because of the lack of experimental data this would add more uncertainties and speculative results. Because of that reason, it was not done in this present work. As an addition, the modeling approach should be further improved by considering an appropriate closure models for each gas structures and also a better treatment of gas core interface so that the flow behavior in the whole region in the device and also particularly the gas distribution can be better predicted.

## Acknowledgments

The experimental work was carried out in the frame of the research project “SAVE” (02NUK023B) financed by the German Federal Ministry of Education and Research (BMBF). Ryan Anugrah Putra received a scholarship from the Indonesian-German Scholarship Programme (IGSP).

## References

- Andersson, B., Andersson, R., Hakanson, L., Mortensen, M., Sudiyo, R., van Wachem, B., 2012. Computational Fluid Dynamics for Engineers. Cambridge University Press, New York.
- Antal, S.P., Lahey, R.T., Flaherty, J.E., 1991. Analysis of phase distribution in fully developed laminar bubbly two-phase flow. *International Journal of Multiphase Flow* 17, 635-652.
- Azizi, S., Ahmadloo, E., Awad, M.M., 2016. Prediction of void fraction for gas-liquid flow in horizontal, upward and downward inclined pipes using artificial neural network. *International Journal of Multiphase Flow* 87, 35-44.
- Burns, A.D., Frank, T., Hamill, I., Shi, J.-M., 2004. The Favre averaged drag model for turbulence dispersion in Eulerian multi-phase flows, ICMF2004, Yokohama, Japan.
- Cai, B., Wang, J., Sun, L., Zhang, N., Yan, C., 2014. Experimental study and numerical optimization on a vane-type separator for bubble separation in TMSR. *Progress in Nuclear Energy* 74, 1-13.
- Hampel, U., Bieberle, A., Hoppe, D., Kronenberg, J., Schleicher, E., Sühnel, T., Zimmermann, F., Zippe, C., 2007. High resolution gamma ray tomography scanner for flow measurement and non-destructive testing applications. *Review of Scientific Instruments* 78, 103704.

- Hosokawa, S., Tomiyama, A., Misaki, S., Hamada, T., 2002. Lateral Migration of Single Bubbles Due to the Presence of Wall. 855-860.
- Ishii, M., Zuber, N., 1979. Drag coefficient and relative velocity in bubbly, droplet or particulate flows. *AIChE Journal* 25, 843-855.
- Kanizawa, F.T., Ribatski, G., 2017. Void fraction and pressure drop during external upward two-phase crossflow in tube bundles – part I: Experimental investigation. *International Journal of Heat and Fluid Flow* 65, 200-209.
- Lucas, D., Krepper, E., Prasser, H.M., 2007. Use of models for lift, wall and turbulent dispersion forces acting on bubbles for poly-disperse flows. *Chemical Engineering Science* 62, 4146-4157.
- Lucas, D., Rzehak, R., Krepper, E., Ziegenhein, T., Liao, Y., Kriebitzsch, S., Apanasevich, P., 2016. A strategy for the qualification of multi-fluid approaches for nuclear reactor safety. *Nuclear Engineering and Design* 299, 2-11.
- Menter, F.R., 1994. Two-equation eddy-viscosity turbulence models for engineering applications. *AIAA Journal* 32, 1598-1605.
- Neumann, M., Schäfer, T., Bieberle, A., Hampel, U., 2016. An Experimental Study on the Gas Entrainment in Horizontally and Vertically Installed Centrifugal Pumps. *Journal of Fluids Engineering* 138, 091301-091301-091309.
- Rusche, H., 2002. Computational fluid dynamics of dispersed two-phase flows at high phase fractions. University of London / Imperial College.
- Rzehak, R., Krepper, E., 2013a. Bubble-induced turbulence: Comparison of CFD models. *Nuclear Engineering and Design* 258, 57-65.
- Rzehak, R., Krepper, E., 2013b. CFD modeling of bubble-induced turbulence. *International Journal of Multiphase Flow* 55, 138-155.
- Schäfer, T., Bieberle, A., Neumann, M., Hampel, U., 2015. Application of gamma-ray computed tomography for the analysis of gas holdup distributions in centrifugal pumps. *Flow Measurement and Instrumentation* 46, 262-267.
- Smirnov, P.E., Menter, F.R., 2009. Sensitization of the SST Turbulence Model to Rotation and Curvature by Applying the Spalart–Shur Correction Term. *Journal of Turbomachinery* 131, 041010-041010.
- Spalart, P.R., Shur, M., 1997. On the sensitization of turbulence models to rotation and curvature. *Aerospace Science and Technology* 1, 297-302.
- Tomiyama, A., Sou, A., Zun, I., Kanami, N., Sakaguchi, T., 1995. Effects of Eötvös number and dimensionless liquid volumetric flux on lateral motion of a bubble in a laminar duct flow. *Multiphase flow* 1995, 3-15.
- Tomiyama, A., Tamai, H., Zun, I., Hosokawa, S., 2002. Transverse migration of single bubbles in simple shear flows. *Chemical Engineering Science* 57, 1849-1858.
- Xue, Y., Li, H., Hao, C., Yao, C., 2016. Investigation on the void fraction of gas–liquid two-phase flows in vertically-downward pipes. *International Communications in Heat and Mass Transfer* 77, 1-8.
- Yin, J., Li, J., Ma, Y., Li, H., Liu, W., Wang, D., 2015. Study on the Air Core Formation of a Gas–Liquid Separator. *Journal of Fluids Engineering* 137, 091301-091301-091309.
- Yin, J., Ma, Y., Qian, Y., Wang, D., 2016. Experimental investigation of the bubble separation route for an axial gas–liquid separator for TMSR. *Annals of Nuclear Energy* 97, 1-6.
- Zhao, Y., Bi, Q., Yuan, Y., Lv, H., 2016. Void fraction measurement in steam–water two-phase flow using the gamma ray attenuation under high pressure and high temperature evaporating conditions. *Flow Measurement and Instrumentation* 49, 18-30.
- Zhu, J., Zhang, H.-Q., 2016. Mechanistic modeling and numerical simulation of in-situ gas void fraction inside ESP impeller. *Journal of Natural Gas Science and Engineering* 36, 144-154.
- Zidouni, F., Krepper, E., Rzehak, R., Rabha, S., Schubert, M., Hampel, U., 2015. Simulation of gas–liquid flow in a helical static mixer. *Chemical Engineering Science* 137, 476-486.

**Table 1**

Distance relative to the entrance of the swirl element.

Position	Distance [mm]
Outlet	240
H6	105
H5	85
H4	65
H3	50
H2	35
H1	20
Inlet	-90

**Table 2**Calculated differential pressure (see **Fig. 3.(a)** and **Fig. 4.(a)**).

$d_B$ [mm]	$\Delta P_{sim} \varepsilon_{in} = 5\%$ [mbar]	$\Delta P_{sim} \varepsilon_{in} = 10\%$ [mbar]
0.5	42	41
1	42	42
2	44	42



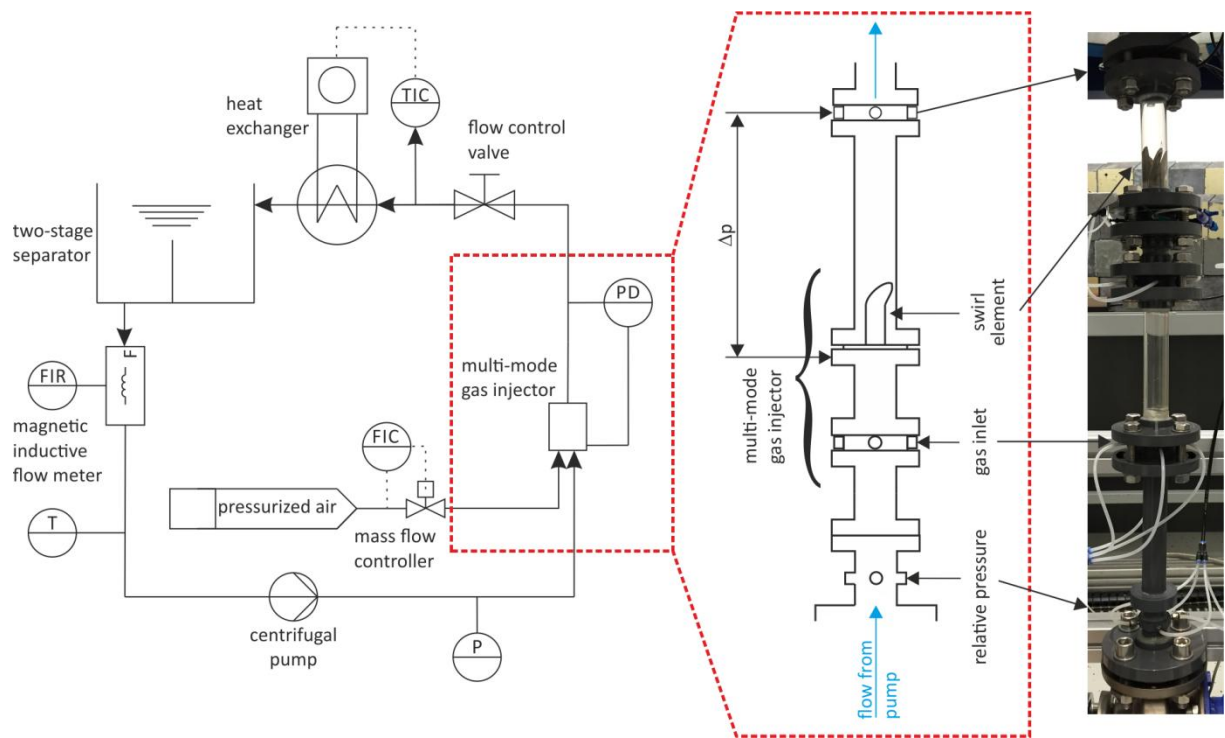


**Fig. 1.** Schematic diagram of experimental apparatus.

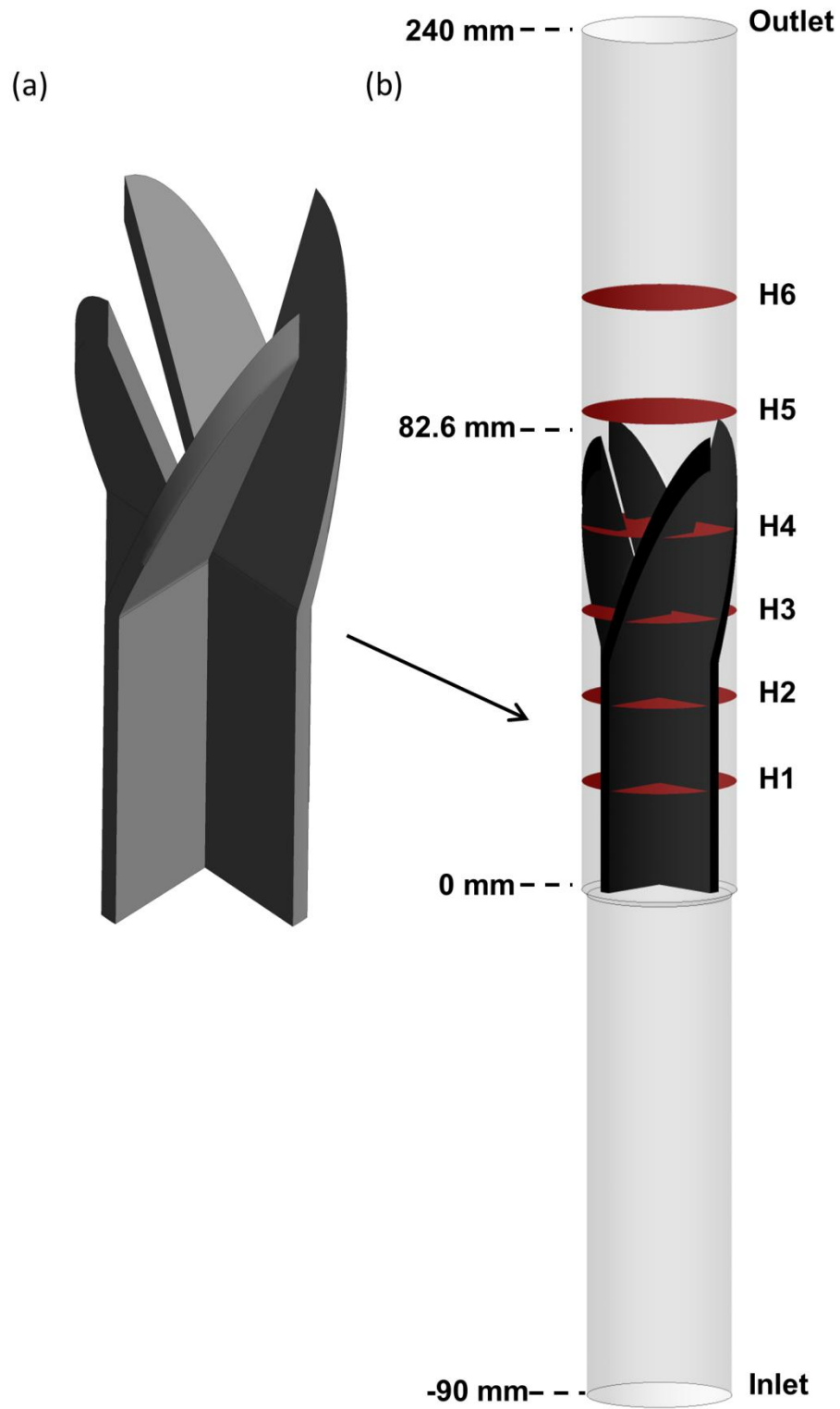


**Fig. 2.** (a) Design of the static swirl element (3D view) and (b) Computational domain including positions for the measurement planes (see **Table 1**).

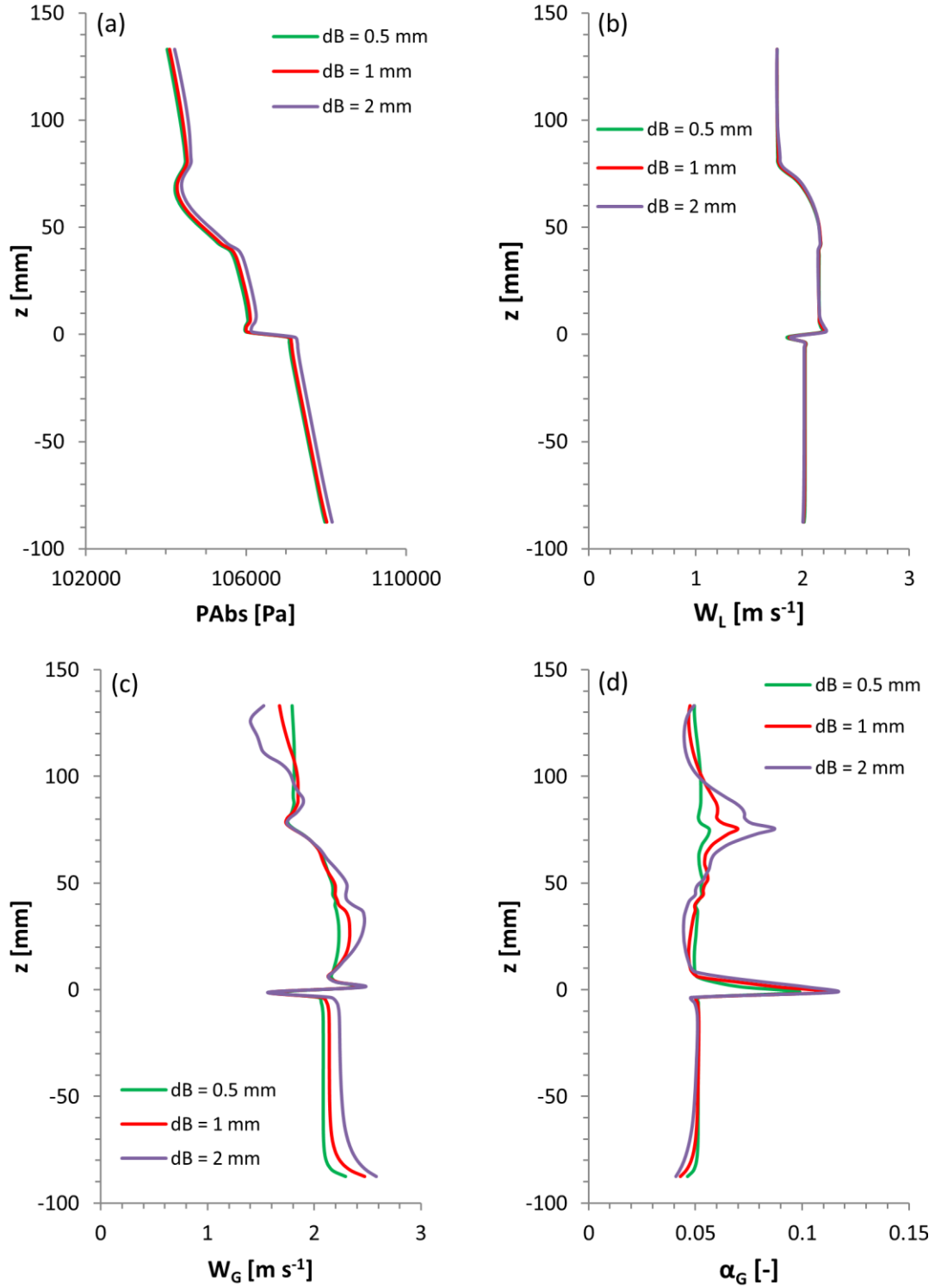


**Fig. 3.** Axial profiles of: (a) pressure, (b) liquid velocity, (c) gas velocity and (d) gas fraction obtained from simulations based on the experiment with inlet gas volume fraction  $\varepsilon_{in} = 5\%$ .

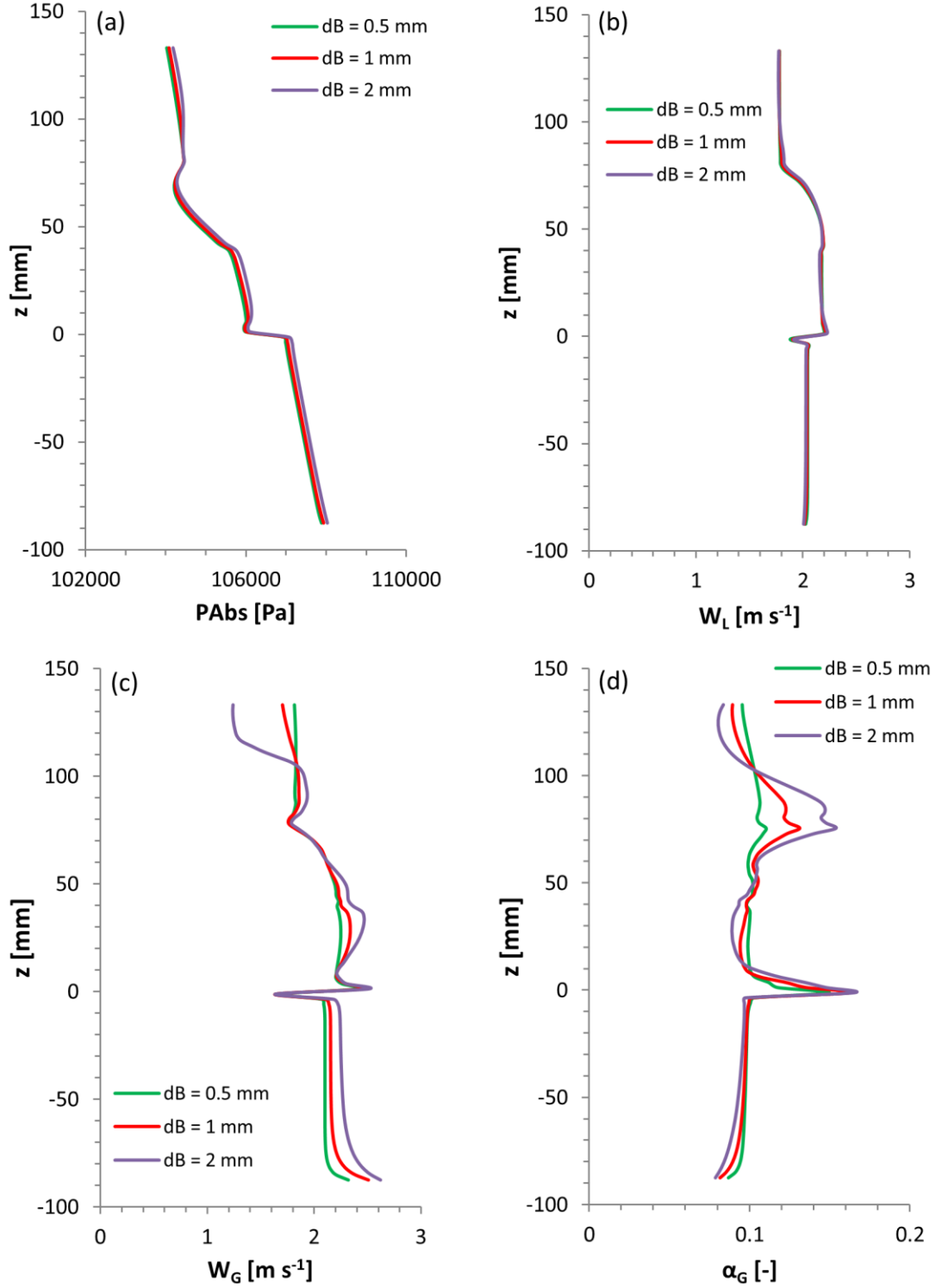


**Fig. 4.** Axial profiles of: (a) pressure, (b) liquid velocity, (c) gas velocity and (d) gas fraction obtained from simulations based on the experiment with inlet gas volume fraction  $\varepsilon_{in} = 10\%$ .

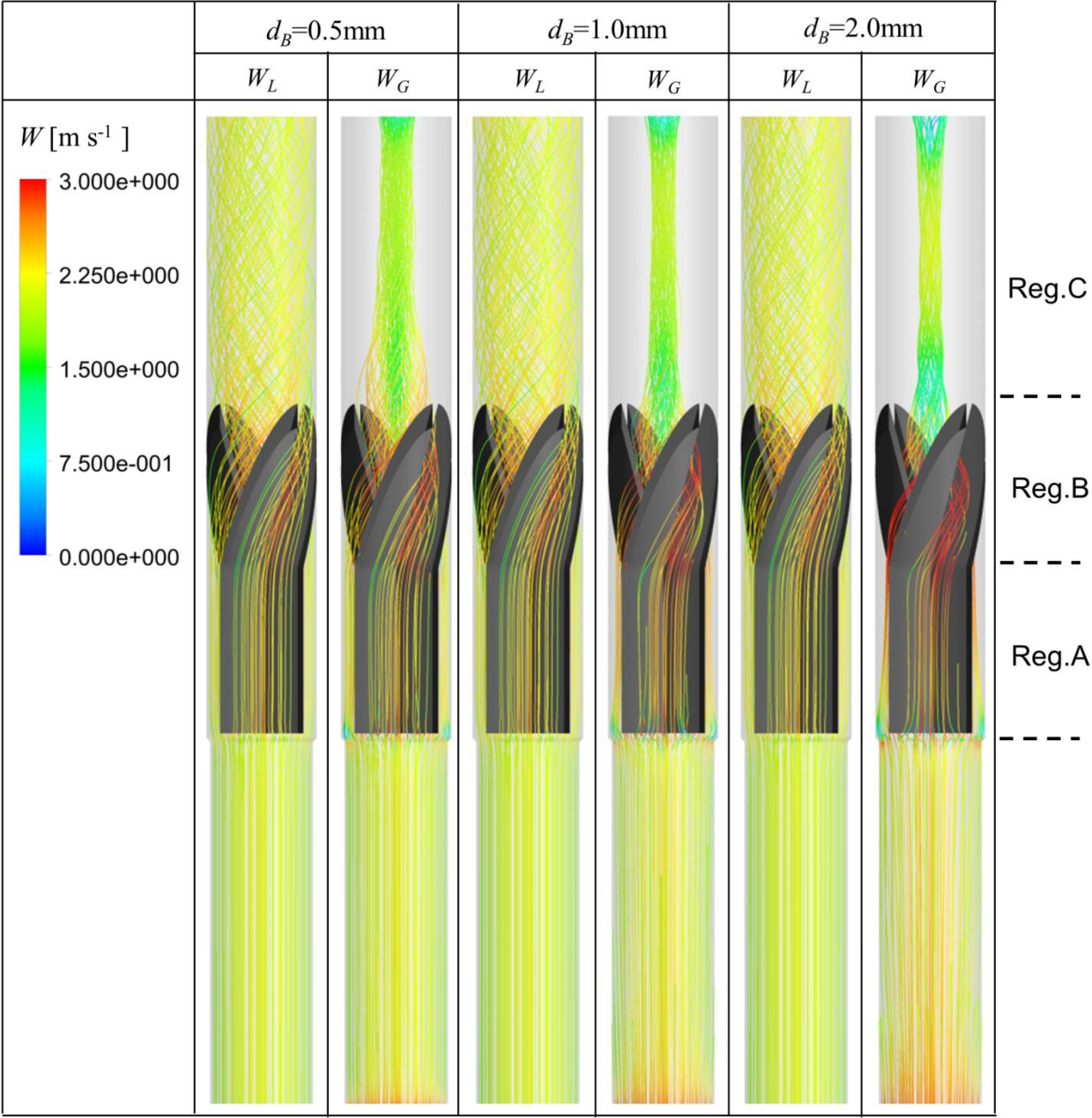


**Fig. 5.** Streamlines of liquid velocity  $W_L$  and gas velocity  $W_G$  for the simulations based on the experiment with inlet gas volume fraction  $\varepsilon_{in} = 5\%$ .

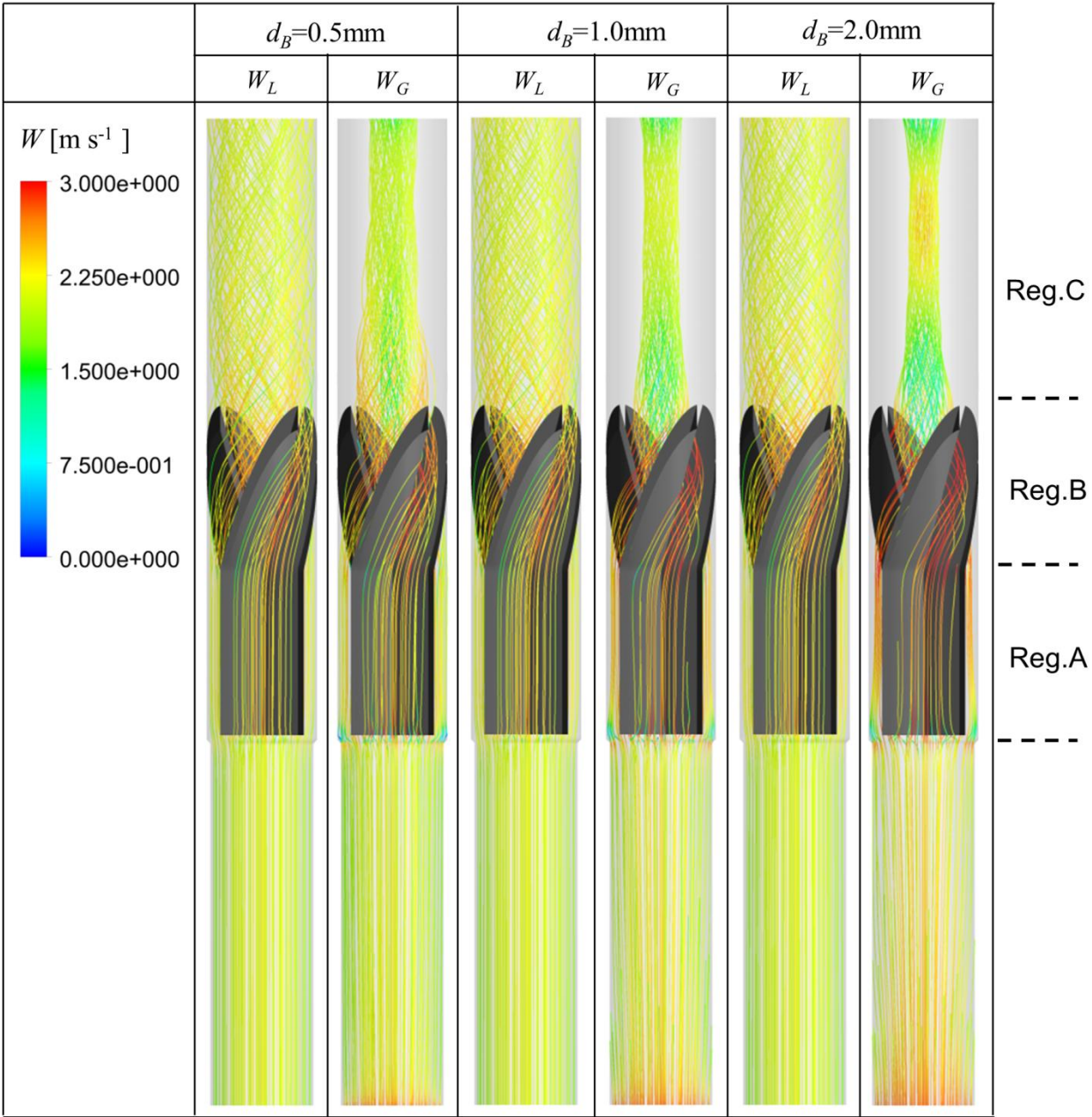


**Fig. 6.** Streamlines of liquid velocity  $W_L$  and gas velocity  $W_G$  for the simulations based on the experiment with inlet gas volume fraction  $\varepsilon_{in} = 10 \%$ .



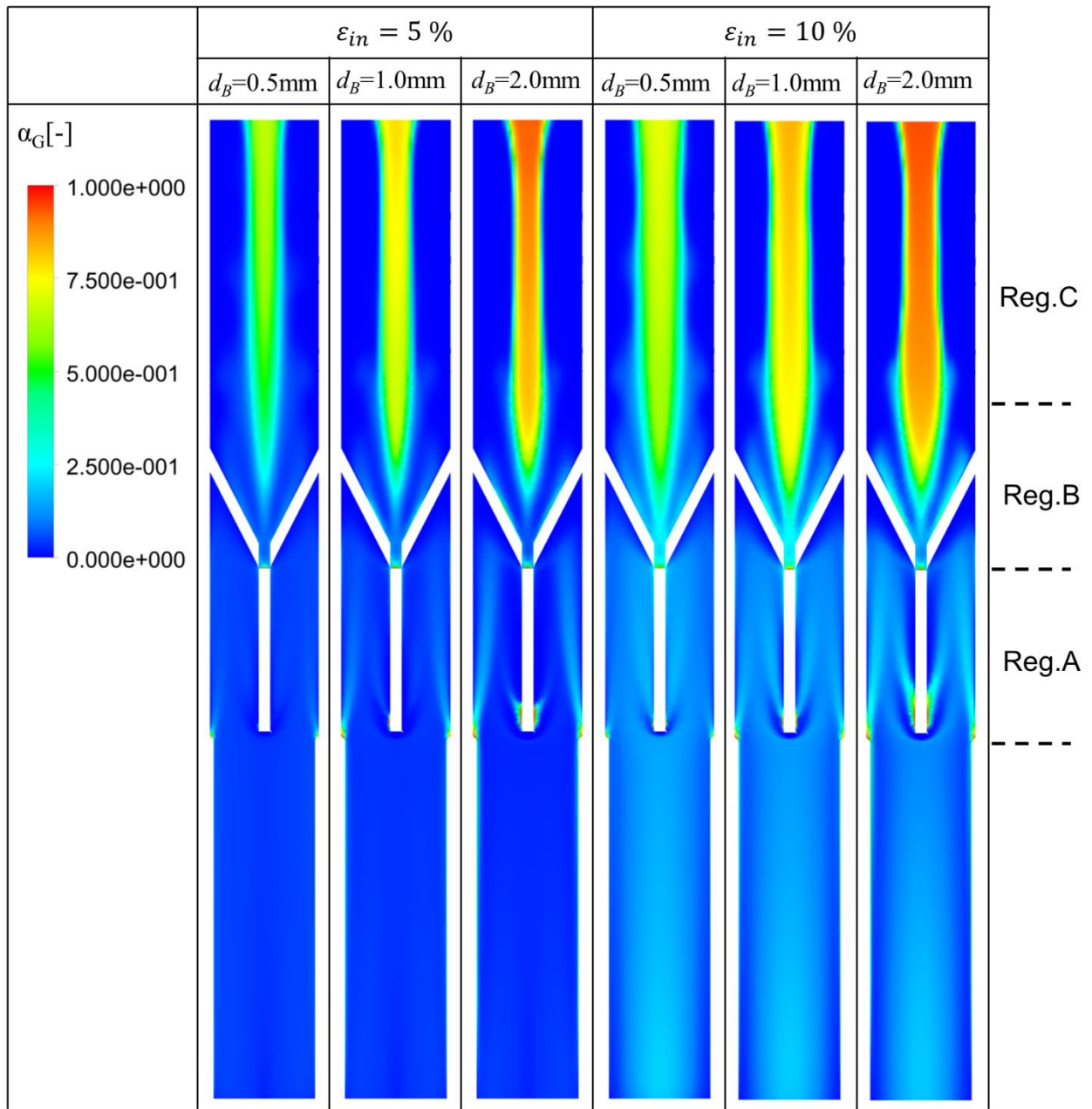


**Fig. 7.** Gas fraction on the central longitudinal plane parallel to the main flow.

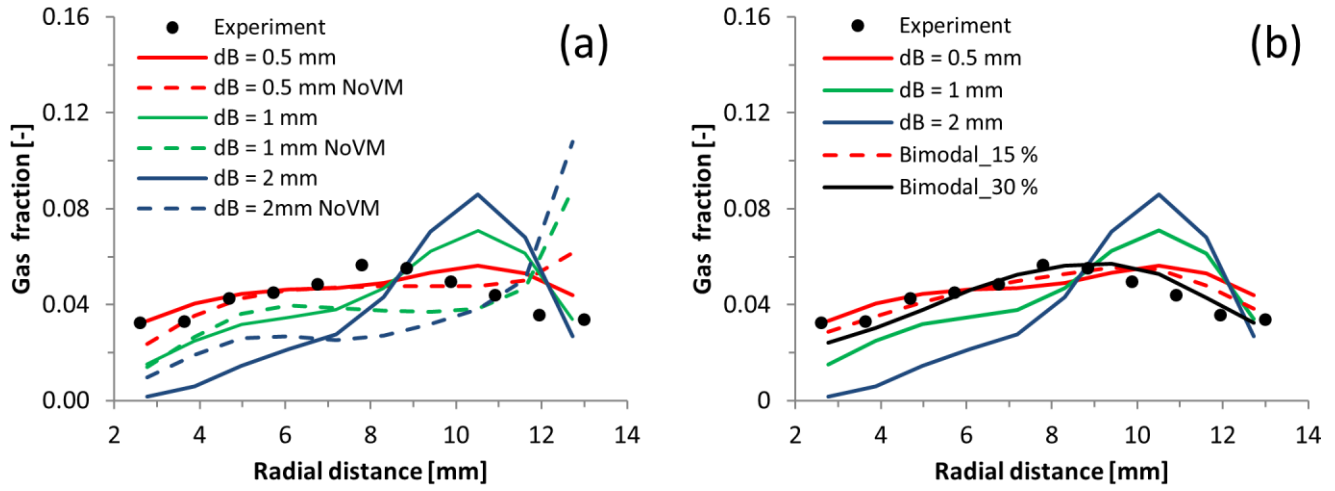


**Fig. 8.** Radial profiles of gas fraction at measurement plane H1 for the inlet gas volume fraction  $\varepsilon_{in} = 5\%$ . (a) Comparison of simulations with and without virtual mass force model. (b) Comparison of simulations assuming mono-disperse and bimodal bubble sizes.



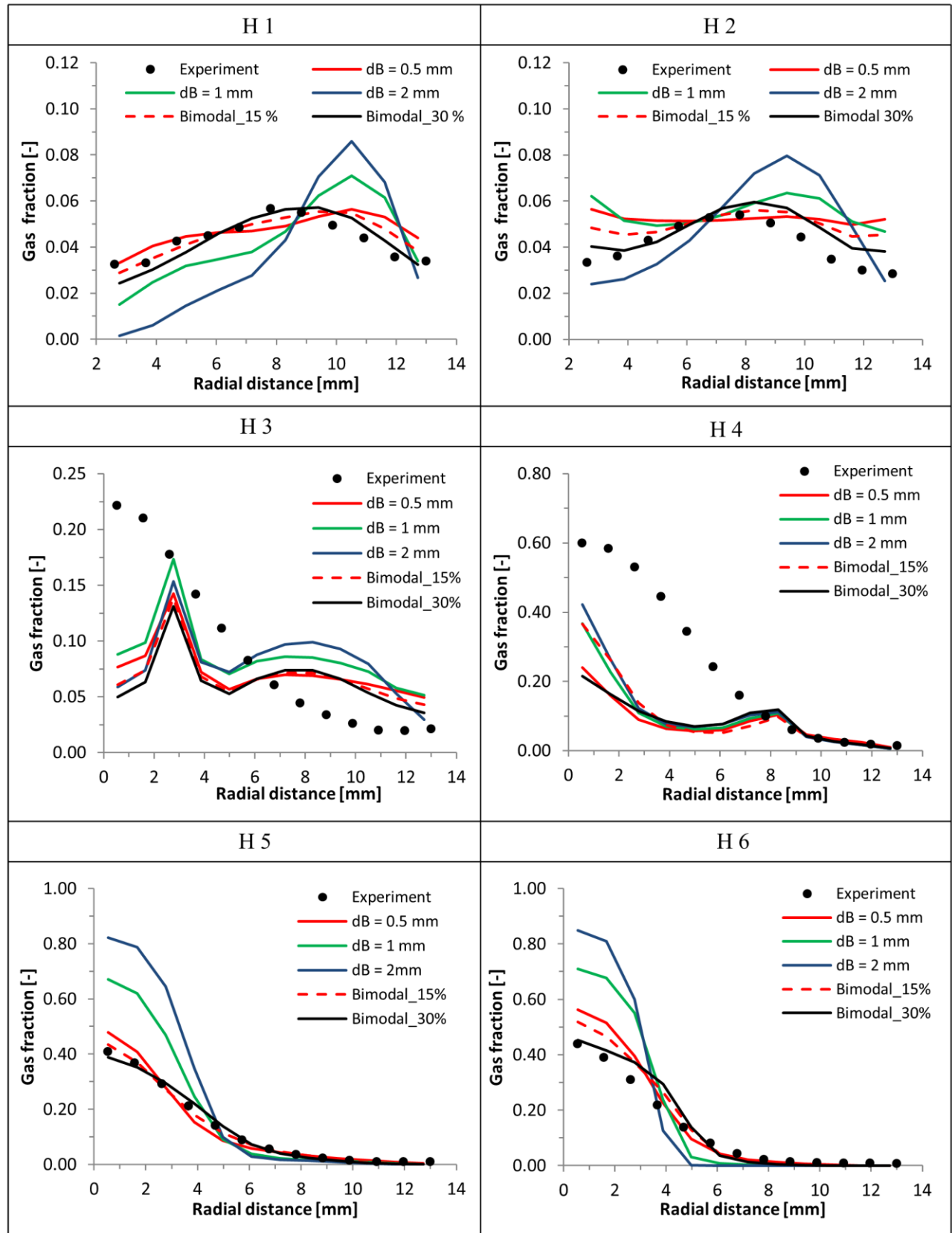


**Fig. 9.** Radial profiles of gas fraction at various measurement planes for the inlet gas volume fraction  $\varepsilon_{in} = 5\%$ .

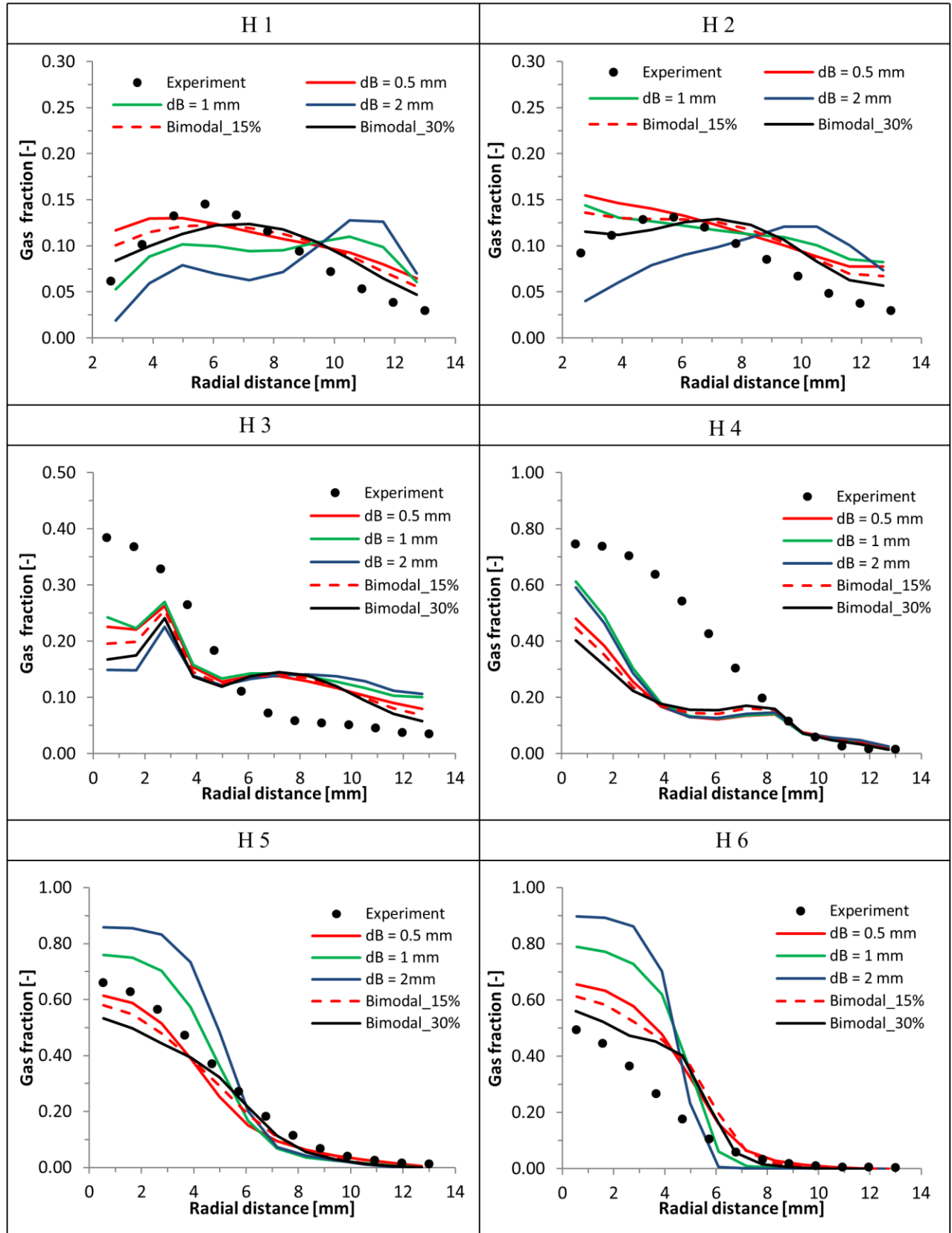


**Fig. 10.** Radial profiles of gas fraction at various measurement planes for the inlet gas volume fraction  $\varepsilon_{in} = 10\%$ .

## References

- Andersson, B., Andersson, R., Hakanson, L., Mortensen, M., Sudiyo, R., van Wachem, B., 2012. Computational Fluid Dynamics for Engineers. Cambridge University Press, New York.
- Antal, S.P., Lahey, R.T., Flaherty, J.E., 1991. Analysis of phase distribution in fully developed laminar bubbly two-phase flow. *International Journal of Multiphase Flow* 17, 635-652.
- Azizi, S., Ahmadloo, E., Awad, M.M., 2016. Prediction of void fraction for gas-liquid flow in horizontal, upward and downward inclined pipes using artificial neural network. *International Journal of Multiphase Flow* 87, 35-44.
- Burns, A.D., Frank, T., Hamill, I., Shi, J.-M., 2004. The Favre averaged drag model for turbulence dispersion in Eulerian multi-phase flows, ICMF2004, Yokohama, Japan.
- Cai, B., Wang, J., Sun, L., Zhang, N., Yan, C., 2014. Experimental study and numerical optimization on a vane-type separator for bubble separation in TMSR. *Progress in Nuclear Energy* 74, 1-13.
- Hampel, U., Bieberle, A., Hoppe, D., Kronenberg, J., Schleicher, E., Sühnel, T., Zimmermann, F., Zippe, C., 2007. High resolution gamma ray tomography scanner for flow measurement and non-destructive testing applications. *Review of Scientific Instruments* 78, 103704.
- Hosokawa, S., Tomiyama, A., Misaki, S., Hamada, T., 2002. Lateral Migration of Single Bubbles Due to the Presence of Wall. 855-860.
- Ishii, M., Zuber, N., 1979. Drag coefficient and relative velocity in bubbly, droplet or particulate flows. *AIChE Journal* 25, 843-855.
- Kanizawa, F.T., Ribatski, G., 2017. Void fraction and pressure drop during external upward two-phase crossflow in tube bundles – part I: Experimental investigation. *International Journal of Heat and Fluid Flow* 65, 200-209.
- Lucas, D., Krepper, E., Prasser, H.M., 2007. Use of models for lift, wall and turbulent dispersion forces acting on bubbles for poly-disperse flows. *Chemical Engineering Science* 62, 4146-4157.
- Lucas, D., Rzehak, R., Krepper, E., Ziegenhein, T., Liao, Y., Kriebitzsch, S., Apanasevich, P., 2016. A strategy for the qualification of multi-fluid approaches for nuclear reactor safety. *Nuclear Engineering and Design* 299, 2-11.
- Menter, F.R., 1994. Two-equation eddy-viscosity turbulence models for engineering applications. *AIAA Journal* 32, 1598-1605.
- Neumann, M., Schäfer, T., Bieberle, A., Hampel, U., 2016. An Experimental Study on the Gas Entrainment in Horizontally and Vertically Installed Centrifugal Pumps. *Journal of Fluids Engineering* 138, 091301-091301-091309.
- Rusche, H., 2002. Computational fluid dynamics of dispersed two-phase flows at high phase fractions. University of London / Imperial College.
- Rzehak, R., Krepper, E., 2013a. Bubble-induced turbulence: Comparison of CFD models. *Nuclear Engineering and Design* 258, 57-65.
- Rzehak, R., Krepper, E., 2013b. CFD modeling of bubble-induced turbulence. *International Journal of Multiphase Flow* 55, 138-155.
- Schäfer, T., Bieberle, A., Neumann, M., Hampel, U., 2015. Application of gamma-ray computed tomography for the analysis of gas holdup distributions in centrifugal pumps. *Flow Measurement and Instrumentation* 46, 262-267.
- Smirnov, P.E., Menter, F.R., 2009. Sensitization of the SST Turbulence Model to Rotation and Curvature by Applying the Spalart–Shur Correction Term. *Journal of Turbomachinery* 131, 041010-041010.
- Spalart, P.R., Shur, M., 1997. On the sensitization of turbulence models to rotation and curvature. *Aerospace Science and Technology* 1, 297-302.
- Tomiyama, A., Sou, A., Zun, I., Kanami, N., Sakaguchi, T., 1995. Effects of Eötvös number and dimensionless liquid volumetric flux on lateral motion of a bubble in a laminar duct flow. *Multiphase flow* 1995, 3-15.
- Tomiyama, A., Tamai, H., Zun, I., Hosokawa, S., 2002. Transverse migration of single bubbles in simple shear flows. *Chemical Engineering Science* 57, 1849-1858.
- Xue, Y., Li, H., Hao, C., Yao, C., 2016. Investigation on the void fraction of gas-liquid two-phase flows in vertically-downward pipes. *International Communications in Heat and Mass Transfer* 77, 1-8.
- Yin, J., Li, J., Ma, Y., Li, H., Liu, W., Wang, D., 2015. Study on the Air Core Formation of a Gas-Liquid Separator. *Journal of Fluids Engineering* 137, 091301-091301-091309.

- Yin, J., Ma, Y., Qian, Y., Wang, D., 2016. Experimental investigation of the bubble separation route for an axial gas–liquid separator for TMSR. *Annals of Nuclear Energy* 97, 1-6.
- Zhao, Y., Bi, Q., Yuan, Y., Lv, H., 2016. Void fraction measurement in steam–water two-phase flow using the gamma ray attenuation under high pressure and high temperature evaporating conditions. *Flow Measurement and Instrumentation* 49, 18-30.
- Zhu, J., Zhang, H.-Q., 2016. Mechanistic modeling and numerical simulation of in-situ gas void fraction inside ESP impeller. *Journal of Natural Gas Science and Engineering* 36, 144-154.
- Zidouni, F., Krepper, E., Rzehak, R., Rabha, S., Schubert, M., Hampel, U., 2015. Simulation of gas–liquid flow in a helical static mixer. *Chemical Engineering Science* 137, 476-486.